AGU100 ADVANCING EARTH AND SPACE SCIENCE

Water Resources Research

RESEARCH ARTICLE
10.1029/2017WR022104

Key Points:
- Spectral coherence analysis revealed drivers of variability in atmospheric evaporative demand across time scales
- Vapor pressure deficit is essential to predicting atmospheric evaporative demand in both energy-limited and water-limited regions
- The effect of small-scale forcing variability on atmospheric evaporative demand depends on driver and dryness

Supporting Information:
- Supporting Information S1

Correspondence to:
L. Peng,
lpeng@princeton.edu

Citation:
Peng, L., Li, D., & Sheffield, J. (2018). Drivers of variability in atmospheric evaporative demand: Multiscale spectral analysis based on observations and physically based modeling. *Water Resources Research*, *54*. https://doi.org/10.1029/2017WR022104

Received 20 OCT 2017
Accepted 22 APR 2018
Accepted article online 25 APR 2018

© 2018. American Geophysical Union. All Rights Reserved.

Drivers of Variability in Atmospheric Evaporative Demand: Multiscale Spectral Analysis Based on Observations and Physically Based Modeling

Liqing Peng[1], Dan Li[2], and Justin Sheffield[1,3]

[1]Department of Civil and Environmental Engineering, Princeton University, Princeton, NJ, USA, [2]Department of Earth and Environment, Boston University, Boston, MA, USA, [3]Department of Geography and Environment, University of Southampton, Southampton, United Kingdom

Abstract Atmospheric evaporative demand (AED) is an important variable linking climate with the terrestrial water cycle and the biosphere. Understanding the dynamics of AED has substantial economic, ecological, and social implications. However, how AED varies at different time scales and the drivers of variability remain elusive. This study used spectral coherence analysis to analyze the relationships between observed and modeled AED and climate drivers across multiple time scales at 228 Chinese stations and explored the cross-scale effects of climate forcings on AED. The results highlight the crucial role of vapor pressure deficit (VPD) in both energy-limited and water-limited regions, therefore models that do not incorporate VPD or underestimate the relative importance of VPD have relatively lower skill in predicting AED. Short-term forcing variability has potential impacts on the long-term AED changes through temperature and associated land-atmosphere feedbacks. Our study implies that model predictions for AED and associated hydrologic impacts may not be valid in a changing climate when the key controls on AED and their relative importance are not appropriately represented.

1. Introduction

Assessment of freshwater availability relies on accurate estimates of water supply and demand (Shiklomanov, 2000; Vörösmarty et al., 2000). Atmospheric evaporative demand (AED) characterizes energetic and atmospheric controls on terrestrial evapotranspiration (ET; Roderick et al., 2007; Wang & Dickinson, 2012), which directly connects climate and the water-energy-food nexus (Conway et al., 2015). Understanding the variability of AED is fundamental to predicting the variability of water demand and quantifying aridity, irrigation, and hydropower production under a changing climate (Stocker, 2014) and has significant economic, ecological, and social impacts. In addition, AED is the primary control on ET and the hydrological cycle in energy-limited regions covering almost half the terrestrial surface (Nemani et al., 2003). It has been widely used as an input to different drought indices and hydrological impact models (Dai, 2013; Greve et al., 2014; Hobbins et al., 2008; Milly & Dunne, 2016; Sheffield et al., 2012; Zhao & Dai, 2015). It can also significantly affect transpiration and forest productivity, which in turn affects the carbon cycle (Novick et al., 2016; Williams et al., 2013).

The drivers of AED variability have motivated numerous studies over past decades, which focus on whether the radiative or atmospheric control dominates the changes in AED (McVicar et al., 2012; Roderick et al., 2009; Roderick & Farquhar, 2002). The classical supply/demand framework (Roderick et al., 2009) provides a concise picture of regional controls on AED, but it only describes the climatology without separating different time scales. AED and its meteorological drivers, including radiation (Wild et al., 2005), vapor pressure deficit (Liu et al., 2004), temperature and humidity (Hobbins et al., 2012), and wind speed (McVicar et al., 2012) vary across a wide range of temporal scales (Dai et al., 1999) depending on atmospheric and land surface conditions. For example, solar radiation changes dramatically from hour to hour by local effects of clouds, although its seasonal pattern is fairly predictable. Temperature and humidity have strong diurnal and seasonal cycles and also change with synoptic weather systems and land-atmospheric interactions over daily to monthly scales (Seneviratne et al., 2006).

Previous studies of the driving factors of AED have focused on one specific time scale using correlations (Matsoukas et al., 2011; Peterson et al., 1995) or attribution analysis (Donohue et al., 2010; Hobbins et al.,

2012; Roderick et al., 2007). However, correlations contain information about both fast (hourly and daily) and slow (seasonal and interannual) processes. In previous attribution analysis methods (e.g., Donohue et al., 2010), the sensitivity of AED to its drivers (the first-order partial derivatives) depends on the long-term average of atmospheric conditions, and thus do not reflect the responses of AED over various scales, especially at short time scales. These weaknesses can be overcome by applying frequency domain techniques, which separate low-frequency and high-frequency variability. Frequency domain analysis has been widely employed to investigate the effect of climate variability on ecosystem water and carbon fluxes (Baldocchi et al., 2001; Ding et al., 2013; Katul et al., 2001; Paschalis et al., 2015) but has not been used to disentangle the intertwining processes controlling AED over multiple time scales, which motivates this study.

AED is often expressed as evaporation rate under an idealized, well-watered situation (Shuttleworth, 1991), which is often called potential evapotranspiration (PET) and/or reference ET. Historically, PET has been a long-established hydrological concept and will be used interchangeably with AED hereinafter. AED is usually estimated from empirical or physically based methods (Federer et al., 1996; McMahon et al., 2013). The empirical methods (often temperature-based) prevail in the literature because the use of physically based models is usually hindered by the lack of surface radiation and wind observations (Milly & Dunne, 2011; Sheffield et al., 2012). Previous studies typically evaluated model skill based on biases and correlations, but models can be tuned to reduce biases and enhance correlations between certain variables, even though the calibration may simply redistribute the error to other model components (the so-called "equifinality" effect, see Beven & Freer, 2001). Given the cross-scale interactions among the drivers of AED, there is a need to assess whether widely used AED models faithfully capture the full spectrum of AED and to identify processes that are critical for modeling AED at various time scales.

The primary goals of this study are (1) to identify the dominant drivers of AED across a range of time scales and (2) to evaluate whether current models can reproduce the temporal dynamics of AED and identify processes that are critical for capturing the full spectrum of AED. In addition, our study also, for the first time, investigates how short-term forcing variability affects AED in the long run using a physically based model. While AED is a hypothetical variable and cannot be measured directly, pan evaporation is often regarded as a surrogate for AED (Roderick et al., 2009). This study focuses on China primarily because of the available pan evaporation data at daily scale (Li et al., 2013; Yang & Yang, 2012). China has a variety of climate conditions and its climate variability is closely linked to monsoons and large-scale atmospheric circulation (Chen et al., 2013). Therefore, a comprehensive study of AED across China not only provides valuable insights into the changing regional climate and hydrology but also has broader implications for other regions (Liu et al., 2010).

This paper proceeds with descriptions of the study region, AED models, the multiscale analysis technique, and experiments (section 2), presentation of the results (section 3), discussion (section 4), and conclusions (section 5).

2. Methods

2.1. The Study Region and Data

In this study, we used daily meteorological data and D20 class pan evaporation measurements provided by the China Meteorological Administration. Complete records (i.e., continuous time series) are required for applying frequency domain analysis (see section 2.3). We selected the period of 1961–2001 during which pan evaporation was continuously monitored (see supporting information Figure S1 and supporting information Text S1 for details). To ensure a balance between relatively complete records and sufficient spatial coverage, we only accepted stations with less than 20% missing data in each month, which leads to a reduction in the number of stations from 485 to 228. Given the very low missing ratio in the original data records ($<$3%, supporting information Figure S1 and supporting information Text S1), we gap-filled the missing data with the last valid record.

Located in the eastern Eurasian Continent, China extends over a large area and has complex topography. Within the country, there is a strong Southeast-Northwest gradient of climate and vegetation conditions. To explore the meteorological drivers under different climates, we divided the country into four climate regions based on the conventional China aridity classification scheme (State Education Commission of the People's Republic of China (SEC), 2011). For convenience, we calculated the dryness index (ϕ = PET/P, the

Table 1
Stations Classified by the Dryness Index[a]

	Humid $0<\phi<2$	Subhumid $2<\phi<4$	Semiarid $4<\phi<8$	Arid $\phi>8$	All
Median dryness	1.22	2.83	5.14	19.68	2.19
Number of stations	100	78	28	22	228

[a]Even though the dryness index (ϕ=PET/P) is an effective way for climate classification, the dryness thresholds rely heavily on the calculation of PET. This study defined the climate regions following the conventional China aridity classification pattern and used pan evaporation to represent PET. Therefore, this standard is different from the UNEP generalized climate classification scheme for Global-Aridity values (1997, http://www.cgiar-csi.org/).

ratio of mean annual potential evapotranspiration [PET] to mean annual precipitation rate, see Budyko, 1974) at each station and defined dryness thresholds as in Table 1 to reproduce a similar pattern as SEC (2011). Figure 1a shows the locations of the 228 stations grouped by the dryness index. Note that we also used observed pan evaporation (Epan) instead of modeled PET in defining the dryness index.

Since AED is driven by radiation, temperature, humidity, and wind speed, we selected five key meteorological variables for evaluation, net radiation (R_n), air temperature (T_a), 2 m wind (u_2), vapor pressure (e_a), and vapor pressure deficit (VPD), which is the difference between the saturation vapor content of air and the actual vapor pressure ($e_s(T_a)-e_a$).

The net radiation (R_n) is calculated as follows (see Appendix A for details):

$$R_n=(1-\alpha_p)R_{sp}+R_{nl} \quad (1)$$

First, the incoming solar radiation (R_s) is computed from the Ångström-Prescott equation with observed sun hours and theoretical day length, following the parameters in McVicar et al. (2007). Second, the incoming solar radiation of the pan (R_{sp}) is estimated based on Yang and Yang (2012) for D20 pan and then used to calculate the net shortwave radiation with a pan albedo of $\alpha_p = 0.14$ (Rotstayn et al., 2006). Third, the net long-wave radiation is estimated from the Stefan-Boltzmann law with correction for humidity and cloud fraction estimated from sun hours, following FAO56 standard formulations (Allen et al., 1998).

Figure 1 presents the annual cycles of pan evaporation and the five meteorological variables under different climates. For each station, we calculated the mean monthly values across 41 years for each variable and normalized them by subtracting the 12 month mean and dividing by the 12 month standard deviation. The

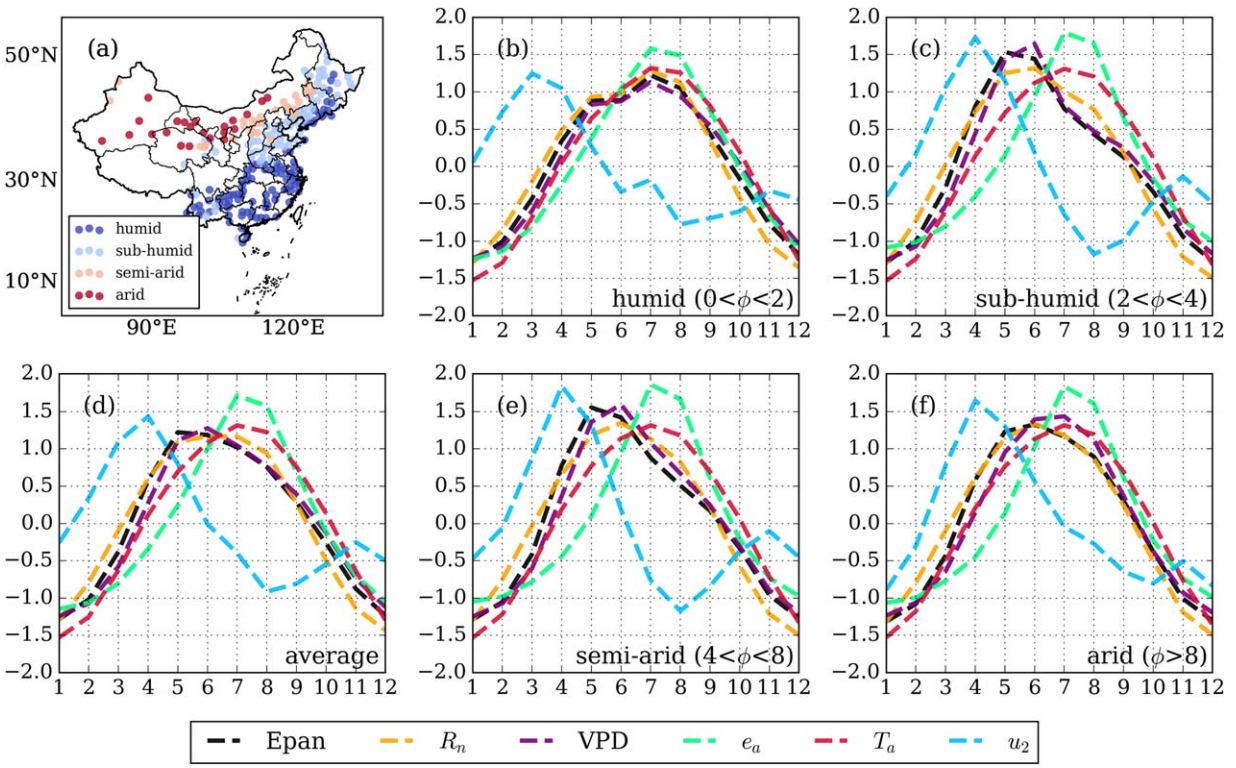

Figure 1. Climatology of Epan and the other key meteorological variables. (a) Spatial distribution of stations grouped by dryness, (d) normalized annual cycles of observed pan evaporation, net radiation (R_n), vapor pressure deficit (VPD), vapor pressure (e_a), air temperature (T_a), and wind averaged across all stations. (b, c, e, and f) Are the same as Figure 1d but for four regions with different dryness indices.

annual cycles of VPD and Epan are very similar to that of R_n (Figure 1d). The peaks of T_a and e_a occur in July, when the East Asian Monsoon brings large amounts of rainfall. Such a lag in temperature and humidity with respect to the seasonal cycle is consistent with other studies in China and the United States (Gaffen & Ross, 1999; Wang & Gaffen, 2001). Wind also has a remarkably distinct seasonal cycle compared to the other variables due to the winter monsoon. From late winter to spring (February–May), northerly winds and cold weather prevail as the Siberian Anticyclone brings cold and dry air from the Arctic. Over most regions, April is the month of maximum wind speed averaged across all stations, which is consistent with prior studies (Chen et al., 2013).

2.2. PET Methods

To examine to what extent the PET models capture the temporal dynamics of pan evaporation, we estimated Epan using five methods driven by the observed meteorological forcing. The five methods include the major types of PET methods, namely, combined method, radiation-based method, and temperature-based method. For the combined method, we selected the Penman method because it is a classical combined approach that estimates PET as the evaporation rate occurring from a wet surface without surface resistance (Penman, 1948; Shuttleworth, 1993). We also selected the Penpan method (Rotstayn et al., 2006) because it is adjusted for pan evaporation from the Penman equation. For D20 class pan evaporation used in this study, we applied the corrections for solar radiation and transfer coefficients in Yang and Yang (2012) and Li et al. (2013). For the radiation-based method, the Priestley-Taylor (PT) method (Priestley & Taylor, 1972) is often used. It describes evaporation from a well-watered surface based on the equilibrium evaporation under conditions of minimal advection; it also represents PET under "potential" atmospheric conditions when water is unlimited (Brutsaert, 2015). Historically, the difficulty of collecting radiation, humidity, and wind speed data has promoted the use of less data-intensive methods (Federer et al., 1996; Lu et al., 2005), such as the temperature-based Thornthwaite method (Thornthwaite, 1948). Here we selected the Turc (1961) and Hamon (1963) methods because they are commonly used and able to use daily data as inputs. Details about each method are listed in Table 2.

2.3. Spectral Coherence Analysis

2.3.1. Coherence

Frequency domain analysis is widely used in signal processing to analyze signals of various frequencies and has been introduced into the hydrologic science (Rodríguez-Iturbe, 1967) and ecological studies (Baldocchi et al., 2001; Katul et al., 2001). The coherence spectrum is a powerful technique to measure the linear correlation structure between two variables across different time scales. It is a frequency domain analog of the correlation coefficient (ρ), while being superior to the correlation because it separates short-term variability from low-frequency signals. In this study, we used the coherence spectrum to describe the relationship

Table 2
Algorithms for Estimating PET

Method and source	Base form	Details
Penman-type Wet surface evaporation	$E_p = E_{pR} + E_{pA}$	E_{pR}: radiative component E_{pA}: aerodynamic component
Penman (1948) Free water evaporation	$E_p = \frac{\Delta}{\Delta+\gamma} \cdot \frac{R_{np}}{\lambda} + \frac{\gamma}{\Delta+\gamma} \cdot E_A$ $E_A = 6.43(1+0.536u_2)D$ (Penman, 1948)	$E_A = f_q(u_2)D$ (drying power of the air)
Penpan (Rotstayn et al., 2006) Pan evaporation	$E_p = \frac{\Delta}{\Delta+a\gamma} \cdot \frac{R_{np}}{\lambda} + \frac{a\gamma}{\Delta+a\gamma} E_A$ (Li et al., 2013; Rotstayn et al., 2006; Yang & Yang, 2012) $E_A = (1.313 + 1.381u_2)D$ (McMahon et al., 2013; Penman, 1956)	$a = f_h(u_2)/f_q(u_2) = 5$ (ratio of the effective surface areas for heat and vapor transfer calculated based on the pan size, based on Yang & Yang, 2012)
Priestley and Taylor (1972)	$E_p = \alpha \frac{\Delta}{\Delta+\gamma} \frac{R_{np}}{\lambda}$	$\alpha = 1.26$ (Priestley-Taylor parameter)
Turc (1961)	RH≥50%: $E_p = 0.013\left(23.88R_{sp}+50\right)\left(\frac{T_a}{T_a+15}\right)$ RH<50%: $E_p = 0.013\left(23.88R_{sp}+50\right)\left(\frac{T_a}{T_a+15}\right)\left(1+\frac{50-RH}{70}\right)$ (McMahon et al., 2013)	
Hamon (1963)	$E_p = 71.55 \cdot \Lambda \cdot e_s/(T_a+273.3)$	Λ: day length in day

Note. Units: The slope of the saturation vapor pressure temperature curve (Δ) in kPa/K, psychrometric constant (γ) in kPa/K, and the latent heat of vaporization of water (λ) in MJ/kg, net radiation of pan (R_{np}) in MJ/m^2/d, incoming solar radiation of pan (R_{sp}) in MJ/m^2/d, vapor pressure deficit (D) in kPa, 2 m wind speed (u_2) in m/s, relative humidity (RH) in %, daily mean air temperature (T_a) in °C, and daily mean saturated vapor pressure (e_s) in kPa.

among observed Epan, modeled Epan and driving variables. Specifically, the coherence spectrum between two series X(t) and Y(t), also called magnitude squared coherence (MSC), is defined as

$$C_{xy} = \frac{|S_{xy}|^2}{S_x \cdot S_y} \tag{2}$$

It is derived from the cross spectrum (S_{xy}) and the power spectral density (S_x, S_y). The power spectral density (S_x) describes the energy intensity of a time series distributed at different frequencies, which is the discrete Fourier transform of the autocorrelation sequence of a time series. The cross spectrum (S_{xy}) is the discrete Fourier transform of the cross correlation between two time series. The MSC is always within the range of 0 and 1. For example, if the pan evaporation solely resonates with VPD, then the MSC between pan evaporation and VPD is expected to be close to 1; their MSC will decrease as the contribution of other variables to pan evaporation increases.

We used a nonparametric method, the Welch's overlapped segment averaging (WOSA) estimator (Welch, 1967) to estimate S_{xy}, S_x, and S_y. Here we focused on a range of periods (reciprocal of frequencies) spanning from 2 to 1,024 days. The highest frequency (the so-called Nyquist frequency) is 2 day, as limited by the sampling resolution. The lowest frequency is constrained by the data length in the segment averaging process (more details are provided in Appendix B). Note that MSC from various realizations can be averaged, without affecting the phase relationship between the two processes. Additionally, MSC is invariant under linear transformation, meaning that bias-correction methods such as simple scaling will not have an influence on the coherence structure. Taking the PT method as an example, adjusting the Priestley-Taylor parameter α as a way of simple scaling has no influence on MSC.

2.3.2. Partial Coherence

The meteorological drivers of AED are not necessarily independent. To partly address this, we invoke partial coherence, which provides a means of separating the effects of multiple variables. Specifically, it is defined as an analog of partial correlation (Rodríguez-Iturbe, 1967):

$$C_{y,a/b} = \frac{|S_{y,a/b}|^2}{S_{y/b} \cdot S_{a/b}} \tag{3}$$

where

$$S_{y,a/b} = S_{ya}\left(1 - \frac{S_{yb} \cdot S_{ab}}{S_{ya} \cdot S_b}\right) \tag{4}$$

$$S_{y/b} = S_y\left(1 - C_{yb}\right) \tag{5}$$

$$S_{a/b} = S_a(1 - C_{ab}) \tag{6}$$

Partial coherence can be seen as the relative improvement of predicting time series Y from time series A beyond considering time series B (Rosenberg et al., 1989). It also has the range between 0 and 1, with 0 indicating the coherence between Y and A is solely because of their relations with B.

2.3.3. Confidence Threshold

In reality, when there are random errors in one or both time series, MSC derived from measurements is never zero even if the two time series are independent and is always smaller than the true coherence (Carter, 1987; Miles, 2011). Thus, one can only state that if the true MSC value is 0, the expected value of measured MSC is within a certain confidence interval corresponding to a certain probability. This is called the confidence threshold or confidence limit for the coherence, estimated by

$$E = 1 - (1 - P)^{\frac{1}{(n_d - 1)}} \tag{7}$$

where P is the probability that MSC is within the interval (0, E), and n_d is the number of independent segments, depending on data length and parameters (Appendix B). Here we used P = 95% significance level for the confidence threshold.

2.4. Traditional Statistical Analysis

To evaluate the skill of the PET models, we also used traditional statistical approaches to quantify the error and correlation between the model predictions and the observations. Three basic statistical quantities are considered: the root-mean-square error (RMSE), correlation coefficient (ρ), and standard deviation (STD).

Table 3
Summary of the Meteorological Input Experiments

	Control experiment	Second experiment	Third experiment
Details	Observed data	Short-term variability in each variable is removed	Randomized with sampling without replacement
Cases	(1)	Moving-average window (1) 7d, (2) 30d	Sampling window (1) 7d, (2) 30d, (3) 90d

Daily modeled Epan were aggregated into multiple time steps (daily, weekly, monthly, and annual) by averaging. Statistics were then computed based on these aggregated time series and summarized using a Taylor diagram (Taylor, 2001), where the distance from a model point to the reference point (1, 1) indicates the relative skill of that model compared to observations.

Although the correlation coefficient and MSC are not directly comparable, they are closely linked because both represent the linear covariability between two time series. For example, the coherence at the annual cycle can be approximately viewed as the correlation coefficient between two detrended monthly time series since both metrics measure the seasonality. Supporting information Table S1 lists ρ and MSC across multiple time scales for comparison.

2.5. Climate Forcing Experiments

To evaluate the cross-scale interactions between meteorological drivers and AED, we conducted several experiments that manipulate the short-term variability of climate inputs to a PET model. Three experiments of generating synthetic climate inputs were considered (Table 3). In the first experiment, observed climate inputs were used to drive the PET model.

In the second experiment, we smoothed out the short-term variability of climate inputs by applying a moving averaging (low-pass filter) to the variable of interest. Four input variables (T_a, R_n, u_2, and e_a) were separately modified and used to generate four Epan series. For each variable, two window sizes were applied. In the first case of a 7 day (7d) moving window, the synthetic input only contains memory of the past three days, so the focus is on the effect of very short-term variations. In the second case of a 30 day (30d) moving window, not only day-to-day, but also week-to-week fluctuations were suppressed, which represents the combined effect of very short-term and medium-term variations within the 30 day period. These scenarios exhibit higher autocorrelation in the modified variables but induce physical inconsistency among variables.

In the third experiment, we carried out a permutation test which breaks down the autocorrelation whilst keeping the cross correlations among all meteorological variables. Given a day of year, we resampled all the climate inputs simultaneously in a moving window. First, all the time indices were shuffled without replacement within a time window across all years. Then the shuffled time series were scaled to match the window-average values of the original time series. For instance, shuffled time series using a 30 day moving window are scaled to match the monthly mean. In this way, the seasonal patterns of the observations are retained by pairing the mean values of original and shuffled time series.

The control experiment provides a benchmark for the other experiments to be compared with. The second experiment focuses on the effect of short-term variability and tests whether Epan dynamics can be predicted from coarser-resolution inputs. The third experiment destroys the autocorrelations in the time series, while partly preserving the seasonal pattern and correlation structure among variables. By employing spectral coherence analysis between the control and the other two experiments, the loss of coherence spectra (1 - MSC) at one frequency can be interpreted as the influence of the modified driver variability on that frequency. This is a useful tool to investigate which cases exhibit stronger cross-scale effects (Paschalis et al., 2015).

3. Results

3.1. Observed Epan-Climate Relationships

3.1.1. Scale-Dependent Correlations Between Epan and Meteorological Variables

Figure 2 summarizes the outcome of the coherence analysis across stations between observed pan evaporation (Epan) and meteorological variables. From the MSC, it can be seen that the dominant driver is vapor

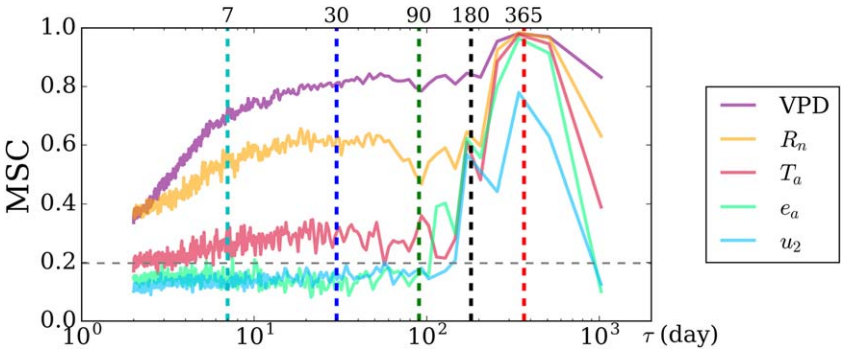

Figure 2. The coherence spectra between Epan and the five meteorological variables. Each curve shows the magnitude squared coherence (MSC) between Epan and each variable, with 95% significance level marked by the horizontal grey dashed line. The *x* axis scale is logarithmic in terms of duration (τ, days), the reciprocal of the frequency. τ specifies the duration of one cycle in a recurring event. Important time scales (weekly, monthly, seasonal, and annual) are marked by the vertical dashed lines. The MSC value of 0.6 between pan evaporation and net radiation (R_n) at $\tau = 30$ day indicates that R_n explains 60% of the variability in pan evaporation at the 30 day period.

pressure deficit (VPD), which accounts for nearly 80% of the variability of AED from weekly (7 days) to semiannual (180 days) scales. The second most important driver is net radiation (R_n), which explains about 60% of the variability in Epan from weekly to semiannual scales. Over these scales, temperature (T_a) has only about 30% on-average similarity with Epan while vapor pressure (e_a) and wind speed have insignificant coherence with Epan (below the 95% confidence limit indicated by the dashed line).

The largest coherence occurs at a period of 365 days with MSC values of 0.9–1.0. This is the annual harmonic mode or the annual cycle, representing the dominant effect of solar forcing on all meteorological variables. Compared to the dominant role of the annual cycle, the longer-term variability in Epan resonates less with the meteorological variables. This might be caused by three factors. First of all, the interannual variations of meteorological variables are usually associated with large-scale oscillations like ENSO (El Niño-Southern Oscillation) and PDO (Pacific Decadal Oscillation). These slow processes tend to induce weaker variability than the seasonal cycle, thereby complicating the detection of similarity between Epan and the drivers. Second, counteractive long-term changes in climate forcing exist. For instance, the warming temperature versus solar dimming or wind stilling has opposite effects on Epan and may result in smaller variability of Epan. Third, the reliability of the low-frequency coherence is questionable given the limited record length, which is one of the caveats of spectral coherence analysis. Although we are interested in the scale dependence of AED changes, decadal variations and long-term trends of AED are beyond the scope of our analysis.

Coherence spectra for scales between 7 and 60 days remain relatively constant. VPD and R_n are still well correlated with Epan at these scales. However, temperature, humidity, and wind speed have very limited effects on Epan over these short scales (Figure 2). The low coherence between Epan and these meteorological variables in this range of time scales is caused by the fast fluctuations of meteorological variables, which arise from weather variability and/or measurement errors. For intermediate time scales (60–120 days), variations in meteorological variables are controlled by both the shifting of the seasonal cycle and synoptic weather systems. As a result, the relations between Epan and driving variables are highly nonlinear across these time scales, as evidenced by the pronounced coherence declines at the period of 90 days.

3.1.2. Interactions Between VPD and R_n

VPD and R_n are the two key driving variables determining the temporal variability of Epan (Figure 2). However, a remaining open question is whether and how VPD modifies the way R_n affects Epan and vice versa. There is a strong correlation between R_n and VPD, evidenced by the fact that the sum of VPD and R_n contributions substantially exceeds unity (Figure 2). At diurnal scales, the time lag between R_n and VPD that causes the diurnal hysteresis between ET and VPD has been observed (Zhang et al., 2014). Yet little work has been done on how the interactions between R_n and VPD affect AED across different climates and time scales. Figure 3e shows that the MSC of R_n-VPD is highly dependent on dryness over short-term to intermediate time scales (from 20 to 180 days). The R_n-VPD coherence remains high in humid regions ($\phi < 2$). At

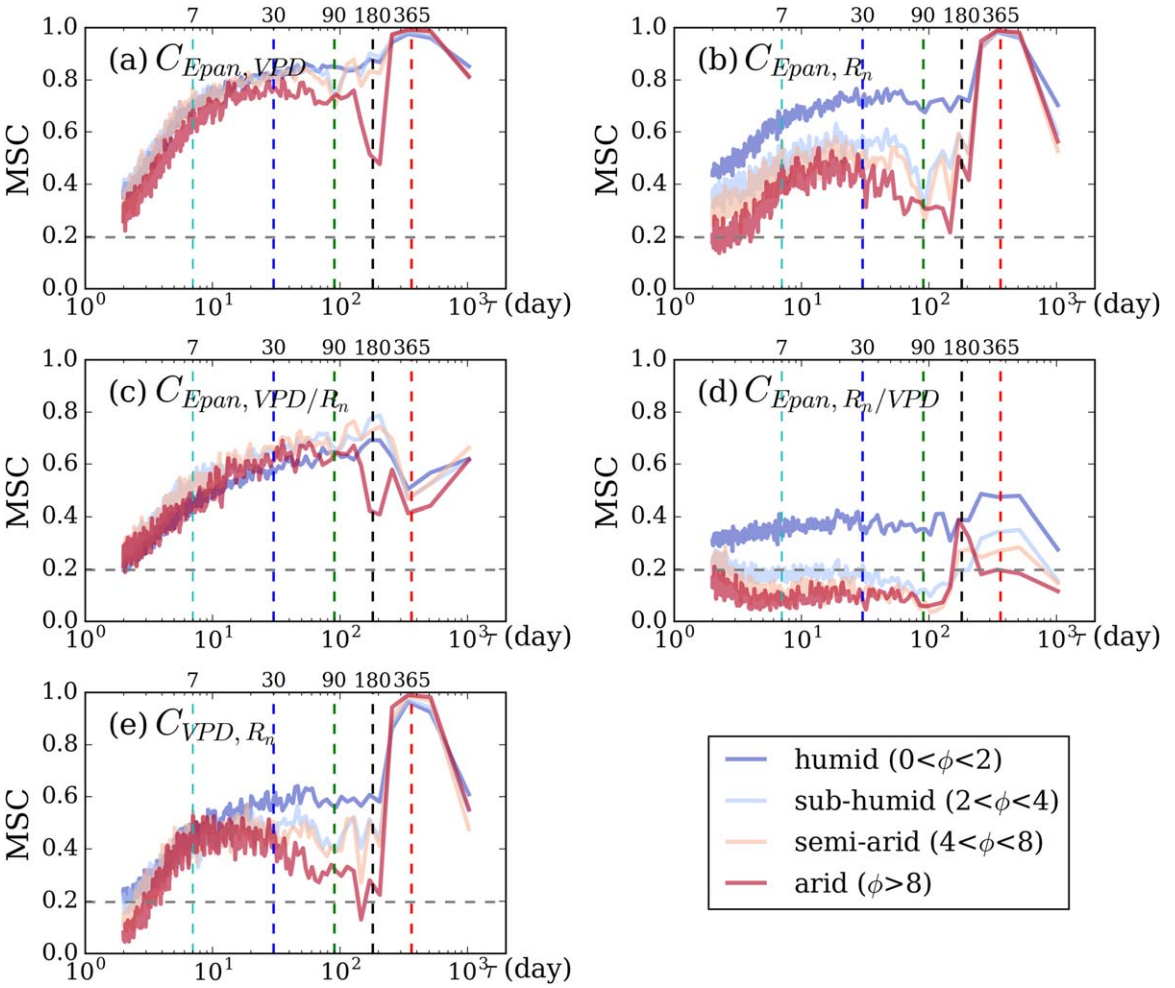

Figure 3. Coherence spectra among Epan, VPD, and R_n. Coherence spectra (a) between Epan and VPD, (b) between Epan and R_n, partial coherence (c) between Epan and VPD excluding R_n, (d) between Epan and R_n excluding VPD, (e) coherence spectra between VPD and R_n. Results are grouped by dryness indices.

daily scale, high radiation loads are often associated with clear sky conditions and low humidity, and thus large VPD. At weekly to monthly scales, high radiation loads are often accompanied by high-pressure systems. During these periods, surface temperature and air temperature are anomalously high and soil moisture is relatively low, which may inhibit large-scale water vapor transport and soil evaporation and increase VPD. In the driest region, there is a significant reduction (increase) in the Epan-VPD (Epan-R_n) correlation on the time scale of 180 days (Figures 3a–3d). This is consistent with the fact that Epan and VPD (R_n) are out-of-phase (in-phase) in the summer time (Figure 1f).

The MSC result indicates that the regulation of R_n on Epan tends to be much stronger in humid regions (Figure 3b). Partial coherence analysis is then employed to separate the independent contributions to Epan of VPD and R_n. After removing the effect of VPD, R_n still has divergent influences on Epan depending on the dryness and these influences remain constant over different time scales (Figure 3d). Most notably, the relative contribution of R_n on Epan is no longer significant in drier regions ($\phi > 2$). Comparing Figure 3b with Figure 3d, we find that the R_n-VPD relation enhances the Epan-R_n coherence from 0.4 to 0.7 (by about 75%) in humid regions, and from insignificant to around 0.4 (by about 3 times) in arid regions. This implies that a considerable fraction of the Epan-R_n correlation is introduced by VPD and the degree that VPD enhances the Epan-R_n correlation depends on dryness.

In contrast, the way VPD affects Epan is found to be similar across all dryness regions over short time scales (<60 days; Figure 3a). When the effect of R_n is excluded (Figure 3c), there is a small reduction in the MSC across scales and the reduction is also similar across all dryness at short time scales. While R_n enhances the

correlation between VPD and Epan, the enhancement is much smaller than the enhancement of Epan-R_n correlation by VPD. Given that the Epan-VPD correlation is much higher than the Epan-R_n correlation (Figures 3a and 3b) and that VPD and R_n are coupled (Figure 3e), including the effect of R_n does not provide as much additional information as the other way around.

3.1.3. The Importance of Temperature and Humidity for VPD and R_n

A surprising result is that the individual contributions of temperature and humidity to Epan are much lower than that of VPD (Figure 2). This implies that VPD should be regarded as an integrated variable for parameterizing AED instead of being separated into air temperature and specific humidity or vapor pressure. The dissimilarity between Epan and T_a is likely due to the exponential relation between saturation vapor pressure and temperature described by the Clausius-Clapeyron equation. At short scales, the contribution of temperature and humidity to VPD tends to increase with dryness (Figures 4a and 4b). This is because in humid regions temperature and humidity are strongly coupled with an MSC of 0.4–0.5 (Figure 4e), leading to high relative humidity and concomitantly small VPD. When variations in VPD are small (humid regions, Figure 1b), temperature and humidity have less influence on VPD and hence Epan, even though the slope of saturation vapor pressure is steeper at high temperature.

The correlation between temperature and R_n (Figure 4c) is much weaker than the VPD-T_a correlation (Figure 4a). The feedback mechanisms inducing such low coherence can vary between regions. In arid regions, warmer temperature induced by higher solar radiation loads may result in increased outgoing long-wave radiation, leading to decreased net radiation ($R_n \uparrow \rightarrow T_s \uparrow \rightarrow R_n \downarrow$). In humid regions, warmer temperature

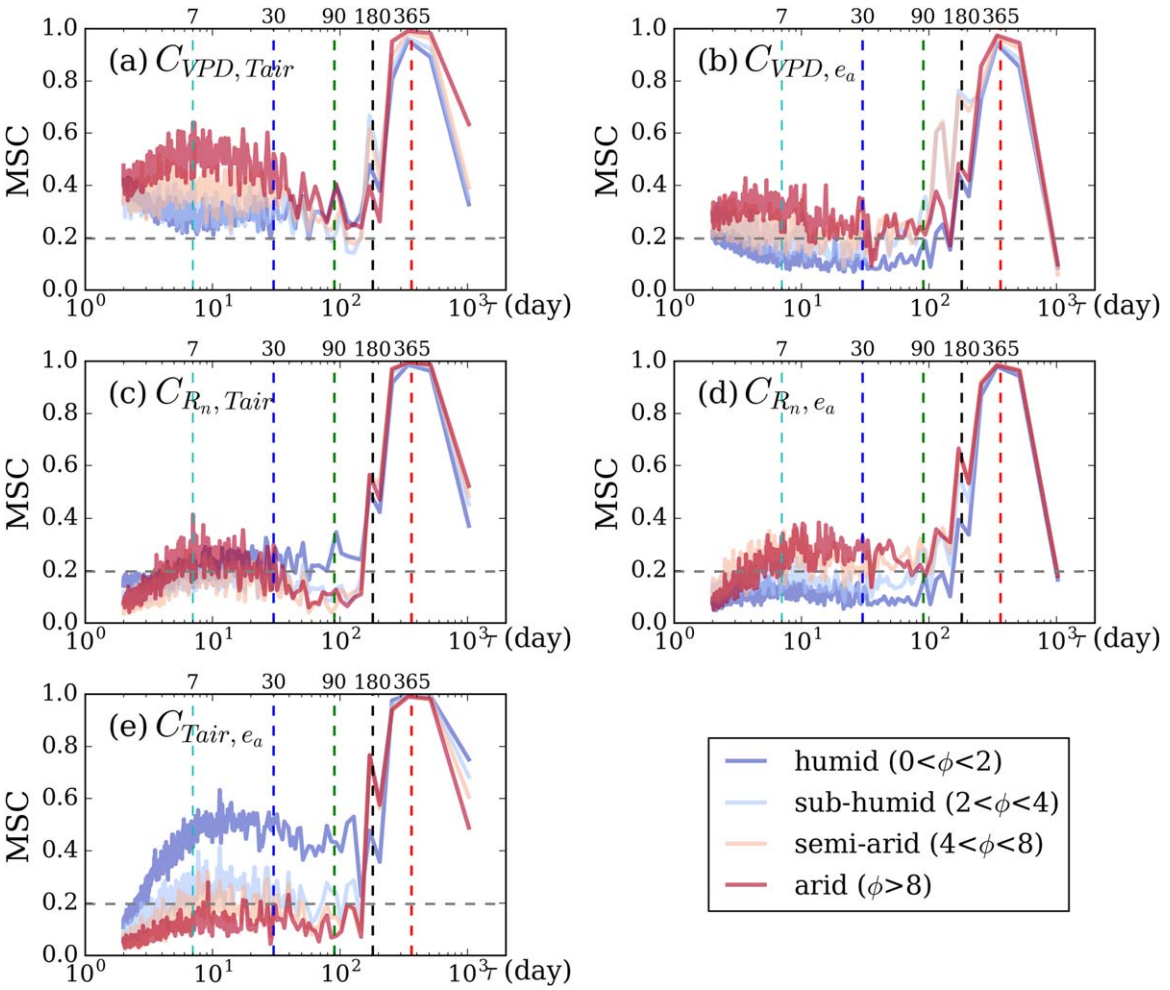

Figure 4. How temperature and humidity affect R_n and VPD. (a, b) Coherence spectra between T_a, e_a, and VPD, (c, d) coherence spectra between T_a, e_a, and R_n, and (e) coherence spectra between T_a and e_a.

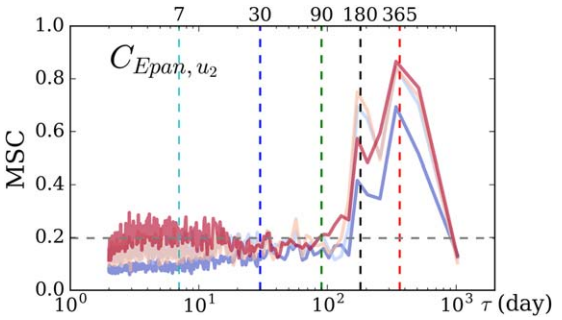

Figure 5. Coherence spectra between Epan and wind speed.

induced by radiation may trigger convection and clouds, and hence less incoming shortwave radiation ($R_n \uparrow\rightarrow T_s \uparrow\rightarrow e_a \uparrow\rightarrow$ clouds $\uparrow\rightarrow R_n \downarrow$). On the other hand, the relatively high R_n-e_a correlation in arid regions (Figure 4d) probably represents a unidirectional component of such a feedback ($R_n \uparrow\rightarrow T_s \uparrow\rightarrow e_a \uparrow$). That is, increased atmospheric water vapor induced by local radiation has little contribution to clouds and precipitation and therefore has limited effect on reducing shortwave radiation.

3.1.4. Wind

Figures 2 and 5 show near-zero associations (below the confidence limit) between Epan and wind on time scales of 30–150 days. Although wind is an important part of the drying power of air and has been suggested to drive the worldwide decreasing trend in Epan (McVicar et al., 2012; Yang & Yang, 2012), the weak coherence at short time scales (<90 days) suggests that the impact of wind on Epan is a highly nonlinear process. In the absence of advection, wind is the main mechanism controlling turbulent diffusion that help remove the escaped water molecules and avoid vapor condensation. In reality, however, advection can take place and the effect of wind on Epan depends on the ambient and upstream moisture conditions. Wind increases evaporation if it transports drier air. In contrast, if moist air is transported, evaporation may be dampened or limited to the equilibrium evaporation, and wind speed plays a small role in modifying evaporation. Other weather events such as cloud condensation and convection may be responsible for the nonlinear Epan-wind relationship as well. In addition, the measured data are daily mean values, which certainly neglect the diurnal variability of wind speed. At seasonal scale, the wind and Epan can be out-of-phase. We found that wind has a distinct seasonal cycle and is also more variable compared to the other variables (Figure 1).

Figure 5 also shows that the wind control on Epan tends to increase along with dryness, which confirms previous studies that show wind has a stronger effect on AED in arid regions of China (Li et al., 2013). Under wet conditions, wind only replaces saturated air with less saturated air, and thus the influence of wind speed on Epan is less significant.

3.2. Evaluation of PET Models

The second goal of this study is to evaluate the performance of PET models across multiple time scales. We focus on comparing traditional metrics such as correlation, which only presents a limited view of covariabilty, with spectral coherence analysis, which provides a full spectrum of correlation between observed Epan and modeled Epan. Additionally, spectral coherence analysis allows us to identify which process causes the model errors at a particular time scale.

3.2.1. Traditional Metrics

First, we used traditional metrics as a baseline evaluation summarized by the Taylor diagram shown in Figure 6. We calculated the basic statistical quantities for observed Epan and modeled Epan averaged across all stations at four temporal scales (daily, weekly, monthly, and annual). We found that the PET methods tend to underestimate the variability of AED at annual time scale, while overestimating the variability of AED at other shorter time scales. The Penpan method has the highest skill, with RMSEs around 1 mm/d and STDs slightly greater than the observation (red lines in Figure 6). Although the Penman and Turc methods have larger variability than the Hamon method, the three methods have comparable RMSEs within the range of 1.5–3.5 mm/d, except at the annual time scale. The PT method has substantially large biases, which overestimates the magnitudes of Epan and enlarges STDs up to 4–6 mm/d. However, these biases can be reduced by adjusting the Priestley-Taylor (PT) coefficient. In terms of covariability, which is an important feature when evaluating the model's capability of capturing temporal variations, the Penpan method has the best performance with correlations (ρ) greater than 0.95 at daily to monthly scales, followed by the Penman method, the Turc method, and the PT method. The Hamon method yields the lowest skill with ρ, implying that it cannot accurately capture the temporal variations of observed Epan.

3.2.2. Metrics Based on Spectral Coherence Analysis

Second, we applied spectral coherence analysis to observed Epan, modeled Epan, and driving variables. Figure 7 shows the coherence between observed and modeled Epan, which yields similar model rankings as

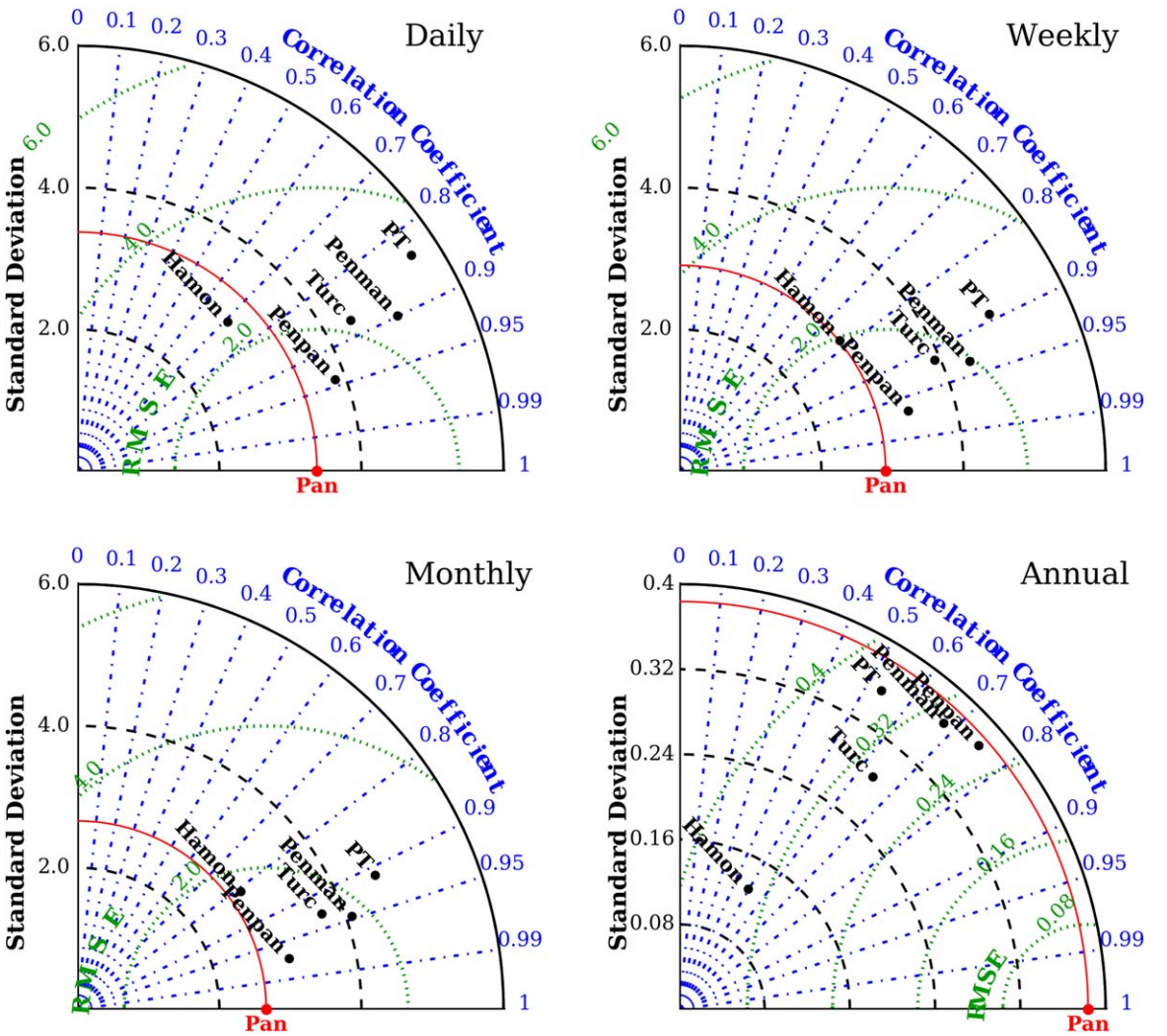

Figure 6. Taylor diagram of daily, weekly, monthly, and annual modeled Epan (Penpan, Penman, Priestley-Taylor, Hamon, and Turc) with respect to Epan. Linear trend of each time series is removed. The units of standard deviation and centered root-mean-square difference (RMSE) are mm/d. The distance between the red dot and the origin denotes the observed standard deviation.

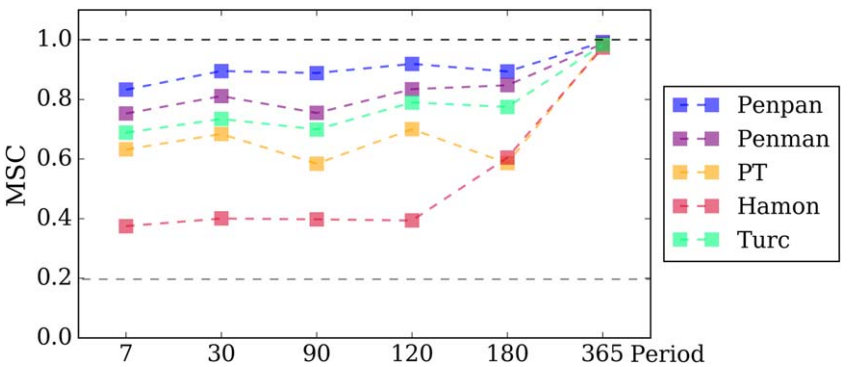

Figure 7. The relationship between the observed and modeled Epan varies across temporal scales. Each line shows the magnitude squared coherence (MSC) between observed pan evaporation and one PET method. We used dashed lines to connect selected periods as they are not continuous on the *x* axis.

the correlations of Figure 6. Coherence spectra between all PET models and observation increase with increasing time scale and reach a peak on the annual scale.

Since spectral coherence analysis only provides a measure of covariability, it can serve as a complementary analysis to traditional metrics such as bias and standard deviation described above. To sum up, the Penpan method is found to be the best model to estimate Epan. The Penman and Turc methods are comparable, given that the Penman method has slightly higher coherence with observations but also higher biases than the Turc method. The large biases in the PT method demonstrate the strong need for calibration. The Hamon method has the lowest skill in reproducing the temporal dynamics of Epan, although its standard deviations are almost identical to the observations and its biases are moderate.

Spectral coherence analysis not only assesses whether the model captures the variations but also can identify the key process (related to a certain variable and at a specific time scale) that causes the model's discrepancy. One major finding is that the success of a model depends on the accurate partitioning of

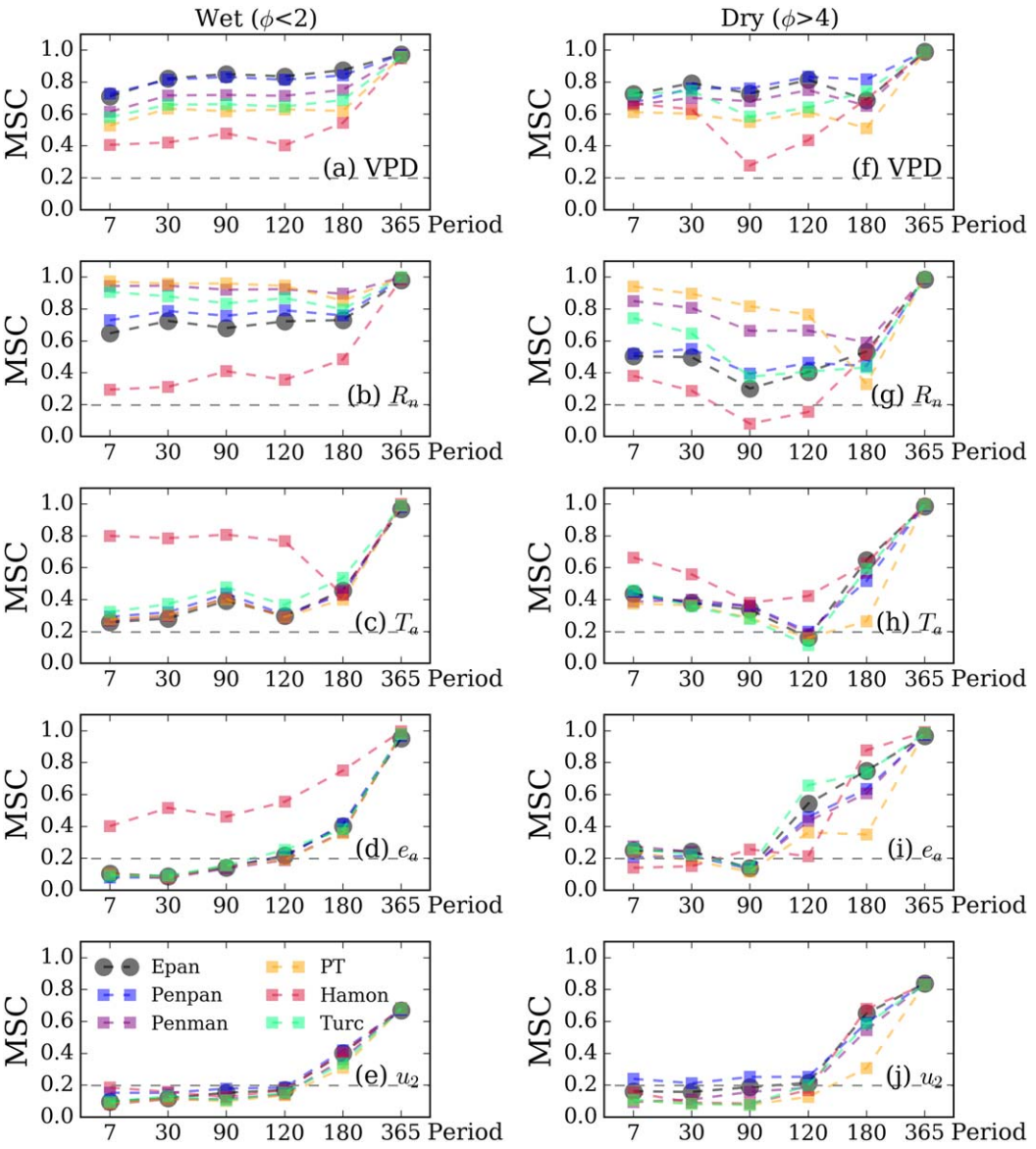

Figure 8. Coherence between the modeled Epan and the meteorological variables in humid regions ($\phi < 2$, on the left column) and dry regions ($\phi > 4$, on the right column). Coherence between observed Epan and driving variables are represented by the grey circles, which refer to the benchmark. A PET method (colored squares) represents a process best if it obtains coherence with the process-related variable closest to observed Epan (grey circles).

radiative and atmospheric control, in other words, the relative importance of R_n and VPD. Figure 8 shows that the Penpan method reproduces both processes very well and therefore has the highest predictability of Epan. The Penman, PT, and Turc methods substantially underestimate the contribution of VPD while they overestimate that of R_n (Figures 8a, 8b, 8f, and 8g). For instance, in humid regions ($\phi < 2$), the modeled Epan from PT and Penman methods have more than 90% similarity with R_n on a range of time scales. In particular, the PT method overestimates the role of R_n by 20%–40% and underestimates the VPD contribution by 20%–30%, which makes the PT method only explain 60%–70% of the observed Epan variability on average.

The partitioning between radiative and atmospheric control becomes unrealistic because of two reasons. The first reason is the lack of key, well-established processes controlling AED. The methods suffering from this issue are mainly the temperature-based or radiation-based methods. These empirical methods tend to distort the sensitivity of AED to its main drivers over short time scales, although they may predict AED well from monthly to annual time scales, for which they were originally developed for. For example, the PT method assumes that the effect of VPD is proportional to the net radiation. In humid regions where VPD is tightly coupled with R_n (Figure 3e), the predictability of the PT method is still reasonable due to the large contribution of R_n. In dry regions ($\phi > 4$), where VPD and R_n are decoupled (Figures 8f–8j), the PT method produces low correlations between modeled AED and the key meteorological variables, particularly over intermediate time scales (90–180 day). Similarly, the Hamon method uses temperature while neglecting the other key variables. Since temperature is tightly coupled with humidity but weakly associated with R_n and VPD in humid regions (see Figure 4), the Hamon method exaggerates the roles of temperature and humidity but underrates the influences of R_n and VPD.

The second reason is the incapability of representing the relative importance of radiative control and atmospheric control. Comparing the Penman and Penpan equations in Table 2, the Penpan equation includes a heat and water vapor transfer ratio that represents the dissimilarity between water vapor and heat transfer. The effective transfer of sensible heat is greater than that of latent heat (water vapor) because of the enhanced heat exchange through the wall of the pan (Linacre, 1994). This ratio increases the importance of water vapor transfer (atmospheric control) and reduces the role of net radiation (radiative control), which better reproduces the observed Epan-R_n and Epan-VPD dynamics, especially for Epan-R_n (Figures 8a, 8b, 8f, and 8g). Although this ratio mainly works for pan evaporation measurement (i.e., not necessarily for PET), it illustrates that capturing the relative importance of radiative and atmospheric control is key for physically based AED modeling.

3.3. Experimental Investigation of the Cross-Scale Effects

Our emphasis has been on identifying the key drivers of Epan variability at multiple scales by examining observations and observation-driven model outputs. However, the above correlation and spectral coherence analysis prevents investigations of nonlinearity and the interplay between short scales and long-term scales. To overcome this limitation, we further developed a model experiment framework to explore the connection between different scales. We constructed a series of synthetic climate inputs that remove or distort the short-term variability (section 2.5). These synthetic inputs were used to force a PET model; spectral coherence analysis was then applied between the model outputs (i.e., the second and third experiments) and those from the same model but forced with observed meteorological variables (i.e., the control experiment). Here we selected the Penpan method because it is fully physically based and our results in section 3.2 indicate that it best reproduces the Epan dynamics across time scales and locations.

In Figure 9, the loss of coherence ($1-\mathrm{MSC}$) between the control experiment and the second experiment (removing the short-term variability) summarizes the influence of the short-term variability of each variable on Epan across time scales. First, it is observed that the influence of short-term variability of meteorological variables will propagate to longer time scales, up to 3 times longer. For example, very short-term variations like day-to-day variability (referred to as the 7d-window scenario) can exert an effect on the 20 day period (supporting information Figure S2), whereas the influence of short-term and medium-term variations (referred to as the 30d-window scenario) can spread up to the 90 day period (supporting information Figure S2).

The response of Epan to the short-term variability of four input variables depends on time scales. Figure 9a shows that the day-to-day variability of R_n, T_a, and wind have significant impacts on weekly cycle (2–7 day)

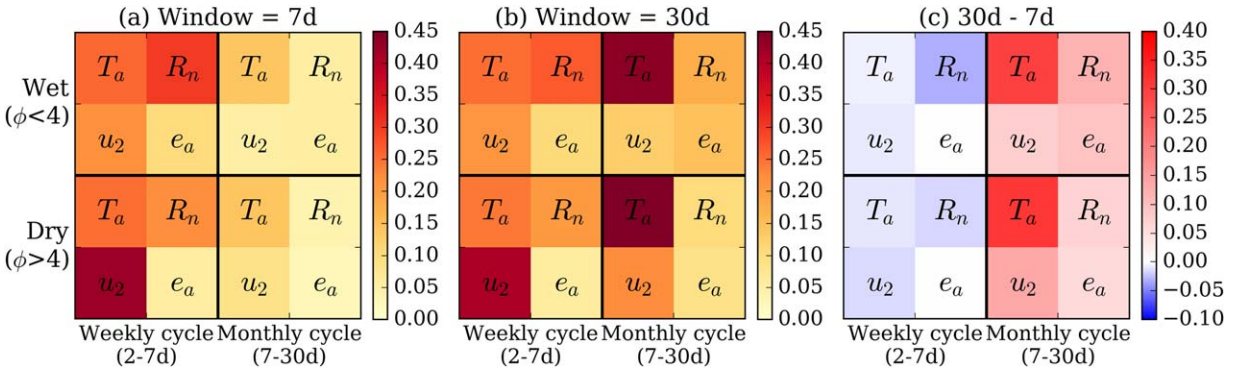

Figure 9. The losses of magnitude squared coherence (1−MSC) between the control experiment and the second experiment (removing the short-term variability) using (a) 7d moving window low-pass filter, (b) 30d moving window low-pass filter, and (c) the differences between Figures 9b and 9a. A higher MSC loss indicates larger influences of short-term variability on Epan dynamics. Each large grid shows the average MSC loss within unique dryness and period bins (see supporting information Figure S2 for all frequencies). Each subgrid represents an experiment where the short-term variability of one driving variable is suppressed.

of Epan variability, while humidity has the least impact (<10%). The differences between Figures 9b and 9a (i.e., Figure 9c) indicate the effects of week-to-week forcing variability. The week-to-week variability of temperature has the strongest influence on monthly cycles (7–30 day) of Epan, which results in more than 30% loss in MSC. The week-to-week variability of R_n, wind, and humidity have moderate influences with 10%–20% losses in MSC. Solar radiation and wind have low persistence because they are fast varying on the daily time scale (Baldocchi et al., 2001; Ding et al., 2013). The response of Epan to the short-term forcing variability also varies with dryness condition (Figure 9, top versus bottom). The way climate affects the importance of different drivers is consistent with our results above: R_n is the dominant driver of Epan in wet conditions, and wind is dominant in dry conditions, whereas the impacts of T_a and e_a (VPD) do not change with climate.

Figure 10 shows the coherence between the control experiment and the third experiment (perturbing short-term variability) with respect to moving window size and dryness. It is found that the impact of eliminating temporal autocorrelation in climate inputs is dramatic (Figure 10). The loss of coherence within the

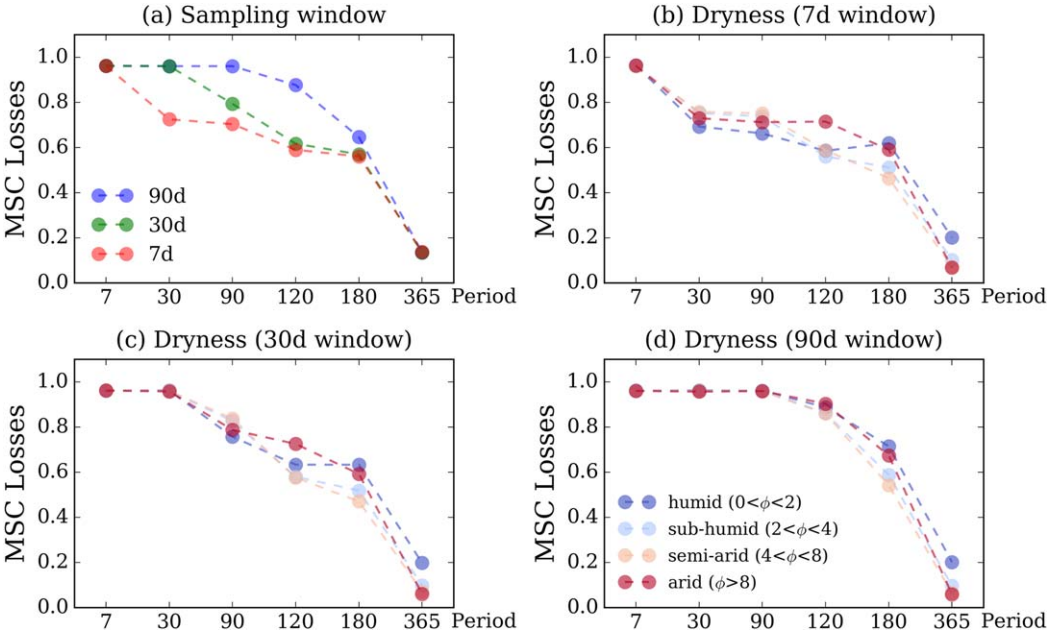

Figure 10. The losses of magnitude squared coherence (1−MSC) between the control experiment and the third experiment (distorting the short-term variability) grouped by (a) size of sampling window, (b) dryness indices using 7d sampling window, (c) dryness indices using 30d sampling window, and (d) dryness indices using 90d sampling window.

period of sampling window is close to 1 (or the coherence declines to almost zero), and it tends to propagate toward longer scales up to the annual cycle. The MSC losses over smaller scales are more sensitive to the sampling window size (Figure 10a), whereas the MSC losses beyond the 180 day scale do not vary with the sampling window size. High coherence on semiannual and annual cycles show that the annual cycles are not distorted with permutations within window sizes smaller than 90 days.

Although the influence of dryness is less important than the sampling window size on short-term to intraseasonal scales (7–90 days), it is found to be important at longer scales (Figures 10b–10d). For example, in the case of 7 day sampling window (Figure 10b), the strongest cross-scale effect is found in the transitional and arid regions on the intraseasonal cycle (30–120 days), and in humid regions beyond the semiannual cycle (180–365 days). Such differences imply that there are two types of dryness-dependent mechanisms linking the short-term and longer-term variability.

The model experiments enable an analysis of how the short-term forcing variability affects long-term variability of AED. However, we are cautious regarding the interpretation of these model experiments, given that these conclusions rely heavily on the model selection. The contradiction between the strong influence of wind speed (Figure 9) and the weak Epan-wind correlation in previous results (Figure 5) suggests a mismatch between measurements and model simulations. In the Penpan method and any Penman-type method, wind conceptually increases Epan or AED by increasing the drying power of air. In reality, the Epan-wind relation is highly nonlinear and the model assumptions could be severely violated when the atmospheric conditions are not uniform and large-scale advection occurs (Figure 5).

4. Discussion

4.1. The Critical Roles of VPD and R_n

Our results confirm that R_n has a stronger influence on AED in humid regions than in arid regions (Figure 3b), which supports the traditional supply/demand framework that changes in actual ET are proportional to the changes in net radiation under energy-limited conditions (Roderick et al., 2009). While the above findings are consistent with expectations, we found that VPD plays a more important role than R_n in capturing the temporal dynamics of AED (Figures 2 and 3). Interestingly, VPD does not lose its control on AED even in energy-limited regions (Figure 3a) where R_n was traditionally thought to be more important. For example, many studies in hydrologic and climate sciences did not consider the role of VPD in energy-limited regions (Seager et al., 2015). The independent contribution of VPD (i.e., excluding the contribution through R_n) does not vary with aridity probably because humidity deficit occurs all the time, and true equilibrium condition is not likely to occur even over wet surfaces (Brutsaert & Stricker, 1979). This is further due to the fact that the atmospheric boundary layer is continually dried out by entrainment from the top of the boundary layer as well as condensation. Such a universal AED-VPD relationship under different climates highlights the unique role of VPD in regulating AED.

We also find that R_n is closely coupled with VPD through temperature and humidity especially in humid regions (Figure 3e). This is not surprising as net radiation integrates the interactions among solar radiation, air temperature, humidity, and cloudiness (Matsoukas et al., 2011; Trenberth et al., 2015). However, the underlying physical process is less certain, as we are not sure whether the R_n-VPD covariability is mainly because weather systems and clouds affect solar radiation, humidity, and DTR (Liu et al., 2010; Peterson et al., 1995) at the same time, or because the changes in temperature and humidity affect long-wave radiation. Understanding the R_n-VPD interactions at different scales, and hence the relation between the surface energy budget and atmospheric conditions, is key to the land-atmosphere feedbacks research with implications for hydrologic extremes studies.

4.2. Model Performance and the Partitioning Between Radiative and Atmospheric Components

As to why some models show degradation in coherence over daily to seasonal scales, even though they can obtain reasonable estimates of long-term AED with moderate biases, we identify that the major issues in these models are (a) the neglect of key controls on AED in their formulations and (b) the incapability to capture the relative importance of radiative control versus atmospheric control.

The Hamon method does not consider energy balance and uses an empirical temperature function to replace radiation. The PT approach, a typical method solely relying on net radiation, does not explicitly take

VPD into account. It assumes that the atmospheric control is proportional to the radiative control. As noted above, VPD has a significant influence in both dry and wet climates; furthermore, the R_n-VPD relation decreases with increasing aridity and only 60% linearity between R_n and VPD is found at wet stations (Figure 3e). Therefore, the PT method has low skill, especially in dry regions (Figure 8). In addition, even though the PT approach predicts the monthly AED well, it is not able to reproduce the short-term variability of AED.

Although methods like Penman and Turc do consider both VPD and R_n, they substantially overestimate the radiative control on pan evaporation, while underestimating the atmospheric control (Figures 8a and 8b). Our results demonstrate that the relative importance of radiative control and atmospheric control is critical to reproducing the short-term dynamics of AED. This not only provides a guideline for model selection but also stresses the need for caution on the model predictions for AED and associated hydrologic impacts when the key controls on AED and their relative importance are poorly represented.

Our study is based on observations of pan evaporation, including using them for model evaluation. An important limitation of this analysis is that pan evaporation in water-limited regions is only approximate to the "apparent" PET, which measures the evaporation rate from a small saturated surface rather than homogeneous well-watered surface and thus does not allow the adjustment of surrounding atmospheric conditions (Brutsaert, 2015). The Penman-type methods can be viewed as estimating "apparent" PET using "nonpotential" atmospheric conditions, which can be much higher than the actual PET under "potential" atmospheric condition. With this in mind, the low coherence between Epan and PET models in water-limited regions does not necessarily imply low coherence between AED and PET models. However, the degree to which the climate/dryness affects the ranking of model performance seems to be smaller than the differences due to the methods and/or the time scales (Figure 8), which indicates that our conclusions related to the methods and time scales are relatively robust.

4.3. Processes Across Time Scales

Our study confirms that different variable-related processes do occur in different ranges of time scales (section 3.3). The second experiment shows that the short-term variability in the forcing variables can propagate to longer time scales (Figure 9 and supporting information Figure S2). The third experiment shows that the persistence in the forcing variables has significant impacts on Epan long-term variability, up to 180 day (Figure 10). Given the fact that atmospheric anomalies can persist only for about 2 weeks (Liu & Avissar, 1999), this result is likely to be related to land surface processes that have relatively long persistence via land-atmosphere coupling. For example, soil moisture limitations and the associated land-atmosphere feedbacks can produce a cross-scale effect on weather systems and atmospheric circulation at time scales of several weeks to months (Koster & Suarez, 2001; Seneviratne et al., 2010).

The cross-scale effect varies with dryness, which is consistent with a recent observational study that found different mechanisms of land-atmosphere feedback under different climates (Tuttle & Salvucci, 2016). Our results indicate that such dependence on dryness is associated with the time scale. On the range of weeks to months, we found that the cross-scale effect tends to increase with dryness (Figures 10b–10d). Liu and Avissar (1999) showed that the time scale of soil moisture persistence increases with aridity and latitude. Based on autocorrelation, soil moisture memory persists about 2–4 months in southeastern China and 3–5 months in northern China. On the semiannual to annual time scales, we found that the cross-scale effect tends to increase with wetness (Figures 10b–10d). In energy-limited regions, the long persistence may be a result of biosphere-atmosphere coupling. For example, a decrease in summer AED reduces radiation and vegetation productivity, which leads to less transpiration and precipitation recycling for the next growing season. However, this radiation-productivity feedback was not significantly detected in a recent study by Green et al. (2017). In water-limited semiarid ecosystems (Laio et al., 2001), there is also a potential for short-term forcing variability to influence root water uptake, actual ET, and vegetation productivity via soil moisture-precipitation feedback (D'Odorico & Porporato, 2004).

5. Conclusions

The processes that control AED are complex because they operate on different time scales and their importance varies between different climates. In this study, the relationships between AED and climate drivers across multiple time scales are analyzed using both observed and modeled pan evaporation. Spectral

coherence analysis is applied to determine the importance of the drivers and the performance of different PET models. The impacts of time scales and climate (represented by the dryness) on the behavior of AED and its drivers have been explored. A series of experiments has been conducted to investigate the cross-scale effect of driving variables on AED using the best model. This study confirms and extends the conventional wisdom of the supply/demand framework to multiple time scales. The role of VPD in observational studies, diagnosis, and model selection is particularly highlighted. The major findings are the following:

1. VPD is the primary driver of AED and a preferred predictor in the attribution of AED changes. The independent contribution of VPD to Epan is not sensitive to dryness over shorter time scales. R_n is the second most important driver of AED and its role highly depends on dryness. A considerable fraction of Epan-R_n correlation is introduced by VPD.
2. Although most PET models can obtain reasonable estimations of AED at coarser temporal resolutions, some of them have difficulty in predicting short-term variability due to (a) the lack of representation of atmospheric control (VPD) and (b) the incapability of reproducing the relative importance of radiative control (R_n) and atmospheric control (VPD).
3. Short-term forcing variability strongly affects daily to seasonal scales but has a limited direct effect on the seasonality and interannual variability of AED, although it might affect long-term AED changes via land-atmosphere and biosphere-atmosphere feedbacks.

Appendix A: Net Radiation of the Pan

Based on equation (1), R_{sp} and R_{nl} need to be estimated. First, incoming solar radiation (R_s, W m^{-2}) is computed from the Ångström-Prescott equation with the observed sun hours and theoretical day length, which has the general form as below:

$$R_s = \left(a + b\frac{n}{N}\right)R_a \tag{A1}$$

where n is the observed duration of sun hours, N is the maximum possible duration of daylight hours, and R_a is the daytime extraterrestrial radiation (W m^{-2}) using the FAO56 approach (Allen et al., 1998). Following the parameters in McVicar et al. (2007) due to high levels of aerosols in China, we use a=0.195, b=0.5125 (McMahon et al., 2013).

Then, the incoming shortwave radiation of a pan (R_{sp}, W m^{-2}) comes from three components: direct, diffuse, and reflected solar radiation. It can be calculated as (Yang & Yang, 2012)

$$R_{sp} = (P_{rad}f_{dir} + 2(1-f_{dir}) + 2\alpha)R_s \tag{A2}$$

where f_{dir} is the fraction of direct radiation depending on cloudiness, P_{rad} is the pan radiation factor, and α is the albedo (0.23 for short grass). According to Rotstayn et al. (2006), f_{dir} is defined as $f_{dir} = 0.11 + 1.31R_s/R_a$. R_{sp} is greater than R_s because of the interception of energy by the pan walls. P_{rad} accounts for the additional direct radiation intercepted by the pan wall and is calculated as $P_{rad} = 1.70 + 0.0003\phi^2$, where ϕ is the latitude in degree (Yang & Yang, 2012).

For a D20 pan, the water surface area is 0.0314 m^2, the wall area is 0.0628 m^2, and the vertical wall is effectively exposed to half of the diffuse and reflected radiation (Linacre, 1994). Therefore, the total diffuse radiation is $[0.5\times0.0628/0.0314\times(1-f_{dir})+(1-f_{dir})]R_s = 2(1-f_{dir})R_s$. For a similar reason, the intercepted reflected radiation is $2\alpha R_s$.

Finally, net long-wave radiation (R_{nl}, W m^{-2}) is estimated from the Stefan-Boltzmann law with correction for humidity and cloud fraction estimated from sun hours, following FAO56 standard formulation (Allen et al., 1998):

$$R_{nl} = \frac{1}{2}\sigma\left(T_{\max}^4 + T_{\min}^4\right)(0.34-0.14\sqrt{e_a})\cdot\left(\frac{1.35R_s}{(0.75+2\times10^{-5}z)R_a} - 0.35\right) \tag{A3}$$

where z is the station elevation (m).

Table B1
Spectral Coherence Analysis Parameters

Parameter	Description	Value
N	Total record length (data points in the time series)	14,975
fs	Sampling frequency	1 day = 1/3,600/24 s^{-1}
Poverlap	Percentage overlap between neighboring segments	50%
Np	Segment length (data points per segment)	1,024
RBW	Resolution bandwidth = fs/Np	1/3,600/24/1,024 Hz
Ns	Number of segments = (N/Np−Poverlap)/(1−Poverlap)	2N/Np−1=28
Nd	Number of independent segments = RBW · N/fs = N/Np	14,975/1,024=14.6
P	Probability of confidence interval	0.95
P_f	Probability of false alarm for coherence detection $P_f=1-P$	0.05
E	Statistical estimate of MSC Significance threshold $E=1-(1-P)^{\frac{1}{(n_d-1)}}$	95% confidence level $E(P=0.95)=0.1974$

Appendix B: Spectral Coherence Analysis

The procedure of coherence computation is to divide the time series into several overlapping segments, remove the linear trend, and compute periodogram using Hanning weighting function for each segment, and then average the individual periodograms to yield an overall spectral estimate. Here the overlapping samples are 50% of the segment length following a common procedure. The optimal segment length is a compromise between estimate reliability (shorter segment length) and frequency resolution (longer segment length). Shorter segment length (Np, i.e., the data points in one segment) increases the number of segments (Ns), which can significantly reduce the bias and the variance of magnitude squared coherence (MSC) estimates, while longer segment length produce better spectral resolution bandwidth (RBW, i.e., the smallest frequency that can be resolved). Specifically, a segment length of size Np produces (Np/2 + 1) frequency bands. Besides, shorter segment length also truncates the lower frequency end of the spectrum. After testing out Np = 256, 512, 1,024, and 2,048, we found that results with Np = 1,024 obtain a balance between low variance and frequency resolution, which cut off the period $\tau > 1{,}024$ day (2.8 year scale) and ensure adequate low frequency (at least annual scale). Given the data at daily resolution, high frequency with the period $\tau <= 1$ day (daily scale) are not available since the highest frequency is one-half the sampling rate, namely, 2 day.

Other parameters in spectral estimates are listed in Table B1. We used $P = 95\%$ significance level for the confidence threshold to distinguish frequencies where MSC or partial coherence are significantly different from 0. Note that the estimates of the cross spectrum are unreliable when the coherence itself is small (Wei, 2006).

Acknowledgments
This research was sponsored by NASA under grant NNX14AB36A. L.Q. Peng thanks Zhenzhong Zeng at Princeton University for discussion and suggestions on the paper. We thank the Editor and three anonymous reviewers for their comments, which helped to clarify several important points in the manuscript. The China Meteorological Administration (CMA) meteorological data sets can be accessed from the China Meteorological Data Service Center (CMDC, http://data.cma.cn/data/cdcdetail/dataCode/SURF_CLI_CHN_MUL_DAY_V3.0.html).

References

Allen, R. G., Pereira, L. S., Raes, D., & Smith, M. (1998). *Crop evapotranspiration—Guidelines for computing crop water requirements* (FAO Irrig. Drain. Pap. 56(97), e156). Rome, Italy: Food and Agriculture Organization of the United Nations.

Baldocchi, D., Falge, E., & Wilson, K. (2001). A spectral analysis of biosphere–atmosphere trace gas flux densities and meteorological variables across hour to multi-year time scales. *Agricultural and Forest Meteorology*, *107*(1), 1–27. https://doi.org/10.1016/S0168-1923(00)00228-8

Beven, K., & Freer, J. (2001). Equifinality, data assimilation, and uncertainty estimation in mechanistic modelling of complex environmental systems using the GLUE methodology. *Journal of Hydrology*, *249*(1), 11–29. https://doi.org/10.1016/S0022-1694(01)00421-8

Brutsaert, W. (2015). A generalized complementary principle with physical constraints for land-surface evaporation. *Water Resources Research*, *51*, 8087–8093. https://doi.org/10.1002/2015WR017720

Brutsaert, W., & Stricker, H. (1979). An advection-aridity approach to estimate actual regional evapotranspiration. *Water Resources Research*, *15*(2), 443–450. https://doi.org/10.1029/WR015i002p00443

Budyko, M. I. (1974). In D. H. Miller (Ed.), *Climate and life*. Cambridge, MA: Academic.

Carter, G. C. (1987). Coherence and time delay estimation. *Proceedings of the IEEE*, *75*(2), 236–255.

Chen, L., Li, D., & Pryor, S. C. (2013). Wind speed trends over China: Quantifying the magnitude and assessing causality. *International Journal of Climatology*, *33*(11), 2579–2590. https://doi.org/10.1002/joc.3613

Conway, D., Archer van Garderen, E., Deryng, D., Dorling, S., Krueger, T., Landman, W., et al. (2015). Climate and southern Africa's water-energy-food nexus. *Nature Climate Change*, *5*, 837–846. https://doi.org/10.1038/nclimate2735

Dai, A. (2013). Increasing drought under global warming in observations and models. *Nature Climate Change*, *3*(1), 52–58. https://doi.org/10.1038/nclimate1633

Dai, A., Trenberth, K. E., & Karl, T. R. (1999). Effects of clouds, soil moisture, precipitation, and water vapor on diurnal temperature range. *Journal of Climate*, *12*(8), 2451–2473. https://doi.org/10.1175/1520-0442(1999)012<2451:EOCSMP>2.0.CO;2

Ding, R., Kang, S., Vargas, R., Zhang, Y., & Hao, X. (2013). Multiscale spectral analysis of temporal variability in evapotranspiration over irrigated cropland in an arid region. *Agricultural Water Management*, *130*, 79–89. https://doi.org/10.1016/j.agwat.2013.08.019

D'Odorico, P., & Porporato, A. (2004). Preferential states in soil moisture and climate dynamics. *Proceedings of the National Academy of Sciences of the United States of America*, *101*(24), 8848–8851. https://doi.org/10.1073/pnas.0401428101

Donohue, R. J., McVicar, T. R., & Roderick, M. L. (2010). Assessing the ability of potential evaporation formulations to capture the dynamics in evaporative demand within a changing climate. *Journal of Hydrology*, *386*(1), 186–197.

Federer, C. A., Vörösmarty, C., & Fekete, B. (1996). Intercomparison of methods for calculating potential evaporation in regional and global water balance models. *Water Resources Research*, *32*(7), 2315–2321. https://doi.org/10.1029/96WR00801

Gaffen, D. J., & Ross, R. J. (1999). Climatology and trends of US surface humidity and temperature. *Journal of Climate*, *12*(3), 811–828.

Green, J. K., Konings, A. G., Alemohammad, S. H., Berry, J., Entekhabi, D., Kolassa, J., et al. (2017). Regionally strong feedbacks between the atmosphere and terrestrial biosphere. *Nature Geoscience*, *10*(6), 410–414. https://doi.org/10.1038/ngeo2957

Greve, P., Orlowsky, B., Mueller, B., Sheffield, J., Reichstein, M., & Seneviratne, S. I. (2014). Global assessment of trends in wetting and drying over land. *Nature Geoscience*, *7*(10), 716–721. https://doi.org/10.1038/ngeo2247

Hamon, W. R. (1963). Computation of direct runoff amounts from storm rainfall. *International Association of Scientific Hydrology Publication*, *63*, 52–62.

Hobbins, M., Wood, A., Streubel, D., & Werner, K. (2012). What drives the variability of evaporative demand across the conterminous United States? *Journal of Hydrometeorology*, *13*(4), 1195–1214. https://doi.org/10.1175/JHM-D-11-0101.1

Hobbins, M. T., Dai, A., Roderick, M. L., & Farquhar, G. D. (2008). Revisiting the parameterization of potential evaporation as a driver of long-term water balance trends. *Geophysical Research Letters*, *35*, L12403. https://doi.org/10.1029/2008GL033840

Katul, G., Lai, C. T., Schäfer, K., Vidakovic, B., Albertson, J., Ellsworth, D., et al. (2001). Multiscale analysis of vegetation surface fluxes: From seconds to years. *Advances in Water Resources*, *24*(9), 1119–1132. https://doi.org/10.1016/S0309-1708(01)00029-X

Koster, R. D., & Suarez, M. J. (2001). Soil moisture memory in climate models. *Journal of Hydrometeorology*, *2*(6), 558–570.

Laio, F., Porporato, A., Ridolfi, L., & Rodriguez-Iturbe, I. (2001). Plants in water-controlled ecosystems: Active role in hydrologic processes and response to water stress: II. Probabilistic soil moisture dynamics. *Advances in Water Resources*, *24*(7), 707–723. https://doi.org/10.1016/S0309-1708(01)00005-7

Li, Z., Chen, Y., Shen, Y., Liu, Y., & Zhang, S. (2013). Analysis of changing pan evaporation in the arid region of Northwest China. *Water Resources Research*, *49*, 2205–2212. https://doi.org/10.1002/wrcr.20202

Linacre, E. T. (1994). Estimating U.S. class A pan evaporation from few climate data. *Water International*, *19*, 5–14.

Liu, Y., & Avissar, R. (1999). A study of persistence in the land-atmosphere system using a general circulation model and observations. *Journal of Climate*, *12*(8), 2139–2153. https://doi.org/10.1175/1520-0442(1999)012<2139:ASOPIT>2.0.CO;2

Liu, B., Xu, M., Henderson, M., & Gong, W. (2004). A spatial analysis of pan evaporation trends in China, 1955–2000. *Journal of Geophysical Research*, *109*, D15102. https://doi.org/10.1029/2004JD004511

Liu, M., Shen, Y., Zeng, Y., & Liu, C. (2010). Trend in pan evaporation and its attribution over the past 50 years in China. *Journal of Geographical Sciences*, *20*(4), 557–568. https://doi.org/10.1007/s11442-010-0557-3

Lu, J., Sun, G., McNulty, S. G., & Amatya, D. M. (2005). A comparison of six potential evapotranspiration methods for regional use in the southeastern United States. *JAWRA Journal of the American Water Resources Association*, *41*(3), 621–633. https://doi.org/10.1111/j.1752-1688.2005.tb03759.x

Matsoukas, C., Benas, N., Hatzianastassiou, N., Pavlakis, K. G., Kanakidou, M., & Vardavas, I. (2011). Potential evaporation trends over land between 1983–2008: Driven by radiative fluxes or vapour-pressure deficit? *Atmospheric Chemistry and Physics*, *11*(15), 7601–7616. https://doi.org/10.5194/acp-11-7601-2011

McMahon, T. A., Peel, M. C., Lowe, L., Srikanthan, R., & McVicar, T. R. (2013). Estimating actual, potential, reference crop and pan evaporation using standard meteorological data: A pragmatic synthesis. *Hydrology and Earth System Sciences*, *17*(4), 1331. https://doi.org/10.5194/hess-17-1331-2013

McVicar, T. R., Roderick, M. L., Donohue, R. J., Li, L. T., Van Niel, T. G., Thomas, A., et al. (2012). Global review and synthesis of trends in observed terrestrial near-surface wind speeds: Implications for evaporation. *Journal of Hydrology*, *416*, 182–205. https://doi.org/10.1016/j.jhydrol.2011.10.024

McVicar, T. R., Van Niel, T. G., Li, L., Hutchinson, M. F., Mu, X., & Liu, Z. (2007). Spatially distributing monthly reference evapotranspiration and pan evaporation considering topographic influences. *Journal of Hydrology*, *338*(3), 196–220. https://doi.org/10.1016/j.jhydrol.2007.02.018

Miles, J. H. (2011). Estimation of signal coherence threshold and concealed spectral lines applied to detection of turbofan engine combustion noise. *The Journal of the Acoustical Society of America*, *129*(5), 3068–3081. https://doi.org/10.1121/1.3546097

Milly, P. C. D., & Dunne, K. A. (2011). On the hydrologic adjustment of climate-model projections: The potential pitfall of potential evapotranspiration. *Earth Interactions*, *15*(1), 1–14.

Milly, P. C. D., & Dunne, K. A. (2016). Potential evapotranspiration and continental drying. *Nature Climate Change*, *6*, 946–949. https://doi.org/10.1038/nclimate3046

Nemani, R. R., Keeling, C. D., Hashimoto, H., Jolly, W. M., Piper, S. C., Tucker, C. J., et al. (2003). Climate-driven increases in global terrestrial net primary production from 1982 to 1999. *Science*, *300*(5625), 1560–1563. https://doi.org/10.1126/science.1082750

Novick, K. A., Ficklin, D. L., Stoy, P. C., Williams, C. A., Bohrer, G., Oishi, A. C., et al. (2016). The increasing importance of atmospheric demand for ecosystem water and carbon fluxes. *Nature Climate Change*, *6*, 1023–1027. https://doi.org/10.1038/nclimate3114

Paschalis, A., Fatichi, S., Katul, G. G., & Ivanov, V. Y. (2015). Cross-scale impact of climate temporal variability on ecosystem water and carbon fluxes. *Journal of Geophysical Research: Biogeosciences*, *120*, 1716–1740. https://doi.org/10.1002/2015JG003002

Penman, H. L. (1948). Natural evaporation from open water, bare soil and grass. *Proceedings of the Royal Society of London Series A*, *193*(1032), 120–145. https://doi.org/10.1098/rspa.1948.0037

Peterson, T. C., Golubev, V. S., & Groisman, P. Y. (1995). Evaporation losing its strength. *Nature*, *377*(6551), 687. https://doi.org/10.1038/377687b0

Priestley, C. H. B., & Taylor, R. J. (1972). On the assessment of surface heat flux and evaporation using large-scale parameters. *Monthly Weather Review*, *100*(2), 81–92.

Roderick, M. L., & Farquhar, G. D. (2002). The cause of decreased pan evaporation over the past 50 years. *Science*, *298*(5597), 1410–1411. https://doi.org/10.1126/science.1075390

Roderick, M. L., Hobbins, M. T., & Farquhar, G. D. (2009). Pan evaporation trends and the terrestrial water balance. II. Energy balance and interpretation. *Geography Compass*, *3*(2), 761–780. https://doi.org/10.1111/j.1749-8198.2008.00214.x

Roderick, M. L., Rotstayn, L. D., Farquhar, G. D., & Hobbins, M. T. (2007). On the attribution of changing pan evaporation. *Geophysical Research Letters*, *34*, L17403. https://doi.org/10.1029/2007GL031166

Rodríguez-Iturbe, I. (1967). *The application of cross-spectral analysis to hydrologic time series* (Hydrol. Pap. 24). Fort Collins: Colorado State University.
Rosenberg, J. R., Amjad, A. M., Breeze, P., Brillinger, D. R., & Halliday, D. M. (1989). The Fourier approach to the identification of functional coupling between neuronal spike trains. *Progress in Biophysics and Molecular Biology*, *53*(1), 1–31. https://doi.org/10.1016/0079-6107(89)90004-7
Rotstayn, L. D., Roderick, M. L., & Farquhar, G. D. (2006). A simple pan-evaporation model for analysis of climate simulations: Evaluation over Australia. *Geophysical Research Letters*, *33*, L17715. https://doi.org/10.1029/2006GL027114
Seager, R., Hooks, A., Williams, A. P., Cook, B., Nakamura, J., & Henderson, N. (2015). Climatology, variability, and trends in the US vapor pressure deficit, an important fire-related meteorological quantity. *Journal of Applied Meteorology and Climatology*, *54*(6), 1121–1141. https://doi.org/10.1175/JAMC-D-14-0321.1
Seneviratne, S. I., Corti, T., Davin, E. L., Hirschi, M., Jaeger, E. B., Lehner, I., et al. (2010). Investigating soil moisture–climate interactions in a changing climate: A review. *Earth-Science Reviews*, *99*(3), 125–161. https://doi.org/10.1016/j.earscirev.2010.02.004
Seneviratne, S. I., Lüthi, D., Litschi, M., & Schär, C. (2006). Land-atmosphere coupling and climate change in Europe. *Nature*, *443*(7108), 205–209. https://doi.org/10.1038/nature05095
Sheffield, J., Wood, E. F., & Roderick, M. L. (2012). Little change in global drought over the past 60 years. *Nature*, *491*(7424), 435–438. https://doi.org/10.1038/nature11575
Shiklomanov, I. A. (2000). Appraisal and assessment of world water resources. *Water International*, *25*(1), 11–32. https://doi.org/10.1080/02508060008686794
Shuttleworth, W. J. (1991). Evaporation models in hydrology. In T. J. Schmugge & J. C. André (Eds.), *Land surface evaporation* (pp. 93–120). New York, NY: Springer. https://doi.org/10.1007/978-1-4612-3032-8_5
Shuttleworth, W. J. (1993). Evaporation. In D. R. Maidment (Ed.), *Handbook of hydrology*. Sydney, Australia: McGraw-Hill.
State Education Commission of the People's Republic of China (SEC). (2011). *Eighth grade geography*. Beijing, China: People's Educational Press. Retrieved from http://old.pep.com.cn/czdl/jszx/jxzt/bs/adly_1_1_1_1_2_2_1_1_1_1/jxfz/jcct/201409/t20140917_1217767.htm
Stocker, T. (Ed.). (2014). *Climate change 2013: The physical science basis: Working Group I contribution to the Fifth assessment report of the Intergovernmental Panel on Climate Change*. Cambridge, UK: Cambridge University Press.
Taylor, K. E. (2001). Summarizing multiple aspects of model performance in a single diagram. *Journal of Geophysical Research*, *106*(D7), 7183–7192. https://doi.org/10.1029/2000JD900719
Thornthwaite, C. W. (1948). An approach toward a rational classification of climate. *Geographical Review*, *38*(1), 55–94. https://doi.org/10.2307/210739
Trenberth, K. E., Zhang, Y., Fasullo, J. T., & Taguchi, S. (2015). Climate variability and relationships between top-of-atmosphere radiation and temperatures on Earth. *Journal of Geophysical Research: Atmospheres*, *120*, 3642–3659. https://doi.org/10.1002/2014JD022887
Turc, L. (1961). Evaluation des besoins en eau d'irrigation, évapotranspiration potentielle. *Annales Agronomiques*, *12*(1), 13–49.
Tuttle, S., & Salvucci, G. (2016). Empirical evidence of contrasting soil moisture–precipitation feedbacks across the United States. *Science*, *352*(6287), 825–828. https://doi.org/10.1126/science.aaa7185
Vörösmarty, C. J., Green, P., Salisbury, J., & Lammers, R. B. (2000). Global water resources: Vulnerability from climate change and population growth. *Science*, *289*(5477), 284–288. https://doi.org/10.1126/science.289.5477.284
Wang, J. X., & Gaffen, D. J. (2001). Late-twentieth-century climatology and trends of surface humidity and temperature in China. *Journal of Climate*, *14*(13), 2833–2845.
Wang, K., & Dickinson, R. E. (2012). A review of global terrestrial evapotranspiration: Observation, modeling, climatology, and climatic variability. *Reviews of Geophysics*, *50*, RG2005. https://doi.org/10.1029/2011RG000373
Wei, W. W. (2006). *Time series analysis: Univariate and multivariate methods*. Boston, MA: Addison-Wesley.
Welch, P. (1967). The use of fast Fourier transform for the estimation of power spectra: A method based on time averaging over short, modified periodograms. *IEEE Transactions on Audio and Electroacoustics*, *15*(2), 70–73. https://doi.org/10.1109/TAU.1967.1161901
Wild, M., Gilgen, H., Roesch, A., Ohmura, A., Long, C. N., Dutton, E. G., et al. (2005). From dimming to brightening: Decadal changes in solar radiation at Earth's surface. *Science*, *308*(5723), 847–850. https://doi.org/10.1126/science.1103215
Williams, A. P., Allen, C. D., Macalady, A. K., Griffin, D., Woodhouse, C. A., Meko, D. M., et al. (2013). Temperature as a potent driver of regional forest drought stress and tree mortality. *Nature Climate Change*, *3*(3), 292–297. https://doi.org/10.1038/nclimate1693
Yang, H., & Yang, D. (2012). Climatic factors influencing changing pan evaporation across China from 1961 to 2001. *Journal of Hydrology*, *414*, 184–193. https://doi.org/10.1016/j.jhydrol.2011.10.043
Zhang, Q., Manzoni, S., Katul, G., Porporato, A., & Yang, D. (2014). The hysteretic evapotranspiration—Vapor pressure deficit relation. *Journal of Geophysical Research: Biogeosciences*, *119*, 125–140. https://doi.org/10.1002/2013JG002484
Zhao, T., & Dai, A. (2015). The magnitude and causes of global drought changes in the twenty-first century under a low–moderate emissions scenario. *Journal of Climate*, *28*(11), 4490–4512. https://doi.org/10.1175/JCLI-D-14-00363.1